

Identification campaign of supernova remnant candidates in the Milky Way. II. X-ray studies of G38.7-1.4

R. H. H. Huang¹, J. H. K. Wu¹, C. Y. Hui^{2,4}, K. A. Seo², L. Trepl³, A. K. H. Kong¹
cyhui@cnu.ac.kr

ABSTRACT

We report on XMM-Newton and Chandra observations of the Galactic supernova remnant candidate G38.7-1.4, together with complementary radio, infrared, and γ -ray data. An approximately elliptical X-ray structure is found to be well correlated with radio shell as seen by the Very Large Array. The X-ray spectrum of G38.7-1.4 can be well-described by an absorbed collisional ionization equilibrium plasma model, which suggests the plasma is shock heated. Based on the morphology and the spectral behaviour, we suggest that G38.7-1.4 is indeed a supernova remnant belongs to a mix-morphology category.

Subject headings: ISM: supernova remnants—X-rays: individual (G38.7-1.4)

1. Introduction

Supernovae (SNe) and their remnants play a crucial role in driving the dynamical and chemical evolution of galaxies (Woosley & Weaver 1995). Each SN produces bulks of heavy elements and disperses them throughout the interstellar medium (ISM) (e.g. Thielemann et al. 1996; Chieffi & Limongi 2004). The shock waves from the SN explosions may also trigger star formation in molecular clouds (Boss 1995). In addition, the blast waves in supernova remnants (SNRs) can accelerate particles to relativistic energies via Fermi-I acceleration (Reynolds 2008), which has long been suggested as a promising acceleration mechanism for Galactic cosmic rays (GCRs). For investigating the role of SNRs as GCR accelerators, it is necessary to ask whether they can account for the entire energy density of CRs in the Milky Way. This is related to the mechanical power provided by the SNe, which in turn is associated with

their event rate. In our Milky Way, the currently known SNR population is far below the expectation based on a event rate of 2 SNe/century (Tammann et al. 1994) and a typical evolution timescale of $\sim 10^5$ yrs (see Hui et al. 2012; Hui 2013). Therefore, deeper searches for Galactic SNRs are certainly needed.

With the much improved spatial and spectral resolution and enlarged effective area, state-of-the-art X-ray observatories like Chandra and XMM-Newton provide powerful tools for studying the shock-heated plasma and the non-thermal emission from the leptonic acceleration in SNRs (Hui 2013; Kang 2013). However, the number of X-ray detected SNRs is still significantly smaller than the corresponding number of detections in the radio. Until now there are 302 SNRs that have been uncovered in the Milky Way: 274 objects recorded in Green (2009) plus 28 objects reported in Ferrand & Safi-Harb (2012), while the number of Galactic SNRs detected in X-rays is about 100¹. Therefore, enlarging the sample of the X-ray detected SNRs would be valuable. Recently, we have initiated an observational campaign for searching and identifying new Galactic SNRs with X-ray telescopes (Hui et al. 2012). Here we re-

¹Institute of Astronomy and Department of Physics, National Tsing Hua University, Hsinchu, Taiwan

²Department of Astronomy and Space Science, Chungnam National University, Daejeon, Korea

³Astrophysikalisches Institut und Universitäts-Sternwarte, Universität Jena, Jena, Germany

⁴Corresponding author

¹<http://www.physics.umanitoba.ca/snr/SNRcat/>

port our detailed X-ray analysis of the another SNR candidate G38.7–1.4.

G38.7–1.4 was first detected as an unidentified object in ROSAT All-Sky Survey (RASS) with an extent of about $12' \times 8'$. This object has a centrally-peaked morphology in X-rays. Cross-correlating with the Effelsberg Galactic Plane 11 cm survey data, G38.7–1.4 is found to positionally coincide with an incomplete radio shell (cf. Figure 1d in Schaudel et al. 2002). A follow-up observation with the Effelsberg telescope at a wavelength of 6 cm revealed a non-thermal radio emission with a spectral index of $\alpha = -0.79 \pm 0.23$. Furthermore, the existence of polarization in the radio shell was reported by Schaudel et al. (2002). All these evidences suggest that G38.7–1.4 is very likely to be a SNR with center-filled X-ray (mixed) morphology. However, the poor spatial resolution ($\sim 96''$) and the limited photon statistic (~ 50 source counts) of RASS data do not allow one to unambiguously confirm its physical nature. Furthermore, the limited energy bandwidth of ROSAT (0.1–2.4 keV) does not allow one to determine whether a possible hard X-ray (>2 keV) component, arising from the interactions of the reflected shocks with the dense ambient medium or alternatively from the synchrotron emission radiated by relativistic leptons, is present in the hard X-ray band. This motivates us to carry out a detailed X-ray studies of G38.7–1.4 with XMM-Newton and Chandra.

Considering the composition of GCRs, leptons only constitute a small proportion. A large fraction of the observed GCRs are hadrons (i.e. proton and heavy ions; cf. Sinnis et al. 2009). Due to the large masses of hadrons, they are not efficient synchrotron emitters. X-ray and radio observations are generally difficult to constrain their presence. On the other hand, the collision of relativistic hadrons can lead to the production of neutral pions which can subsequently decay into γ -rays (Caprioli 2011). For complementing the aforementioned X-ray investigation of G38.7–1.4 as a possible acceleration site of GCRs, we have also conducted a search for γ -ray emission at the location of G38.7–1.4 with the Large Area Telescope (LAT) on board the Fermi Gamma-Ray Space Telescope.

In this paper, we report a detailed high energy

investigation of G38.7–1.4. The observations and the data reduction of XMM-Newton and Chandra observatories are described in section 2. Sections 3 and 4 present the results of the X-ray spatial and spectral analysis respectively. In section 5, we describe a deep search of γ -ray emission with Fermi. Finally, we discuss the physical implications of the results and summarize our conclusions in sections 6 and 7 respectively.

2. Observations & Data Reduction

2.1. XMM-Newton Observation

We have observed G38.7–1.4 with XMM-Newton on April 19, 2012 (ObsID: 0675070401) for a ~ 20 ks total exposure. In this observation, the EPIC MOS1/2 and PN instruments were operated in full-frame mode using the medium filter to block optical stray light. All the data were processed with the XMM-Newton Science Analysis Software (SAS) package (Version 11.0.0). Calibrated event files for the MOS1, MOS2, and PN detectors were produced using the SAS task *emchain* and *epchain*, following standard procedures. Events spread at most in two contiguous pixels for the PN (i.e., pattern = 0–4) and in four contiguous pixels for the MOS (i.e., pattern = 0–12) have been selected. We further cleaned the data by accepting only the good time intervals (GTIs) when the sky background was low for the whole camera (< 2.6 counts s^{-1} for MOS1 and MOS2, < 20 counts s^{-1} for PN). The effective exposure times after background cleaning for MOS1, MOS2, and PN are 11.0 ks, 12.3 ks, and 11.2 ks, respectively. Data analyses were restricted to the 0.5–10.0 keV energy band.

2.2. Chandra Observation

We have also observed G38.7–1.4 with Chandra on 2012 June 9–10 (ObsID 13770) using Advanced CCD Imaging Spectrometer (ACIS-I) with a frame time of 3.2 s. The total exposure time is ~ 28 ks. The data was configured in the VFAINT telemetry mode. Data reduction and analysis were processed with Chandra Interactive Analysis Observations (CIAO) version 4.5 software and the Chandra Calibration Database (CALDB) version 4.5.5.1. The level-2 data with background cleaning was used in our study. Data analysis was restricted to the energy range of 0.5 – 8.0 keV.

3. Spatial Analysis

Figure 1 and Figure 2 display the X-ray color image of G38.7–1.4 as observed by Chandra in the energy range of 0.5–8 keV and XMM-Newton in the energy range of 0.5–10 keV respectively. These two images were created by using an adaptive smoothing algorithm with a Gaussian radius of $\leq 10''$ in order to probe the detailed structure of the diffuse emission. A center-filled X-ray morphology has been revealed. The angular extent of G38.7–1.4 as seen in X-ray is $\sim 8' \times 6.6'$ (major axis and minor axis of the dashed ellipse illustrated in Fig. 1).

For investigating the radio counterpart of G38.7–1.4 we extracted the radio data taken with the Very Large Array (VLA) on August 18, 1996 from the NRAO Science Data Archive. These continuum observations were collected at a central frequency of 1.4 GHz in the VLA’s D configuration. After standard cleaning process, a calibrated radio image of G38.7–1.4 is shown in Figure 3 left panel. This incomplete radio shell along the southern part of G38.7–1.4 is consistent with that taken with the Effelsberg radio telescope at 11 cm (Schaudel et al. 2002). In this VLA radio map, apart from the diffuse emission, we noted an extended bright radio feature around the center of the FoV. For comparing the radio and X-ray features of G38.7–1.4, we overlaid the radio contours on the XMM-Newton MOS1/2 image (see Figure 3 right panel).

For searching the counterpart of G38.7–1.4 in the other wavelengths, we have also explored the infrared data obtained by Wide-field Infrared Survey Explorer (WISE; Wright et al. 2010) and H α image downloaded from the Southern H-alpha Sky Survey Atlas (SHASSA; Gaustad et al. 2001). No possible diffuse infrared and H α emission associated with G38.7–1.4 was found in our study.

The sub-arcsecond resolution of Chandra enables us to search for the possible stellar remnant associated with G38.7–1.4. By means of the wavelet source detection algorithm (CIAO tool: *wavdetect*), we searched for the point sources in the whole ACIS-I data. The exposure variation across the detector was accounted by the exposure map. We set the detection threshold such that no more than one false detection caused by background

fluctuation is in the whole field. The lower limit of source significance was set to be $4\sigma_G$, where σ_G is Gehrels error. 21 sources were detected and marked by white circles in Figure 1. The properties of these sources are given in Table 1. Based on the ratio between the source extents and the estimates of the PSF sizes at their position reported by *wavdetect*, most of these sources are found to be point-like except for Sources 13, 17 and 20. However, in view of their coincidence with the diffuse remnant emission, such ratios can possibly be overestimated.

To investigate if these X-ray sources are promising isolated neutron star candidates, we focused on those coinciding with the remnant emission (Source IDs: 13, 17, 19, 20) and proceeded to search for their possible optical counterparts since the X-ray-to-optical flux ratio (f_x/f_{opt}) provides a rudimentary parameter for discriminating the nature of the source. For an isolated neutron star, f_x/f_{opt} is typically larger than 1000 (cf. Haberl 2007) while for field stars and active galactic nuclei the ratio are much lower than the typical < 0.3 and < 50 , respectively (Maccaro et al. 1988; Stocke et al. 1991). By cross-correlating the X-ray sources with the SIMBAD and NED databases and the VizieR catalogue service, we searched for the possible optical counterparts within a search radius of 2 arcsec around each source. Among all these four sources, only Source 19 has an optical counterpart (USNO-B1.0 0944-0406013) identified. For the other three sources without optical counterparts found in this search, we computed their limiting X-ray to optical flux ratios. The X-ray to optical flux ratio is defined as $\log(f_x/f_{opt}) = \log f_x + 5.67 + 0.4R$ (Green et al. 2004), where R is the R-band magnitude and f_x is derived in the 0.5–2.0 keV. Since these X-ray sources are too faint for spectral fitting, we crudely estimated their X-ray fluxes in the 0.5–2.0 keV energy range from the count rates with the aid of WebPIMMS by assuming a weighted average column density of $N_H = 1.0 \times 10^{22} \text{ cm}^{-2}$ toward G38.7–1.4 from the HI survey by Kalberla et al. (2005) and an absorbed power-law spectrum with $\Gamma = 1.8$. Taking the limiting magnitude of the USNO-B1.0 catalog (i.e. $R > 21$), the limiting X-ray to optical flux ratios of Sources 13, 17 and 20 are found to be > 0.25 , > 0.26 and > 0.32 respectively. These values are not constraining in

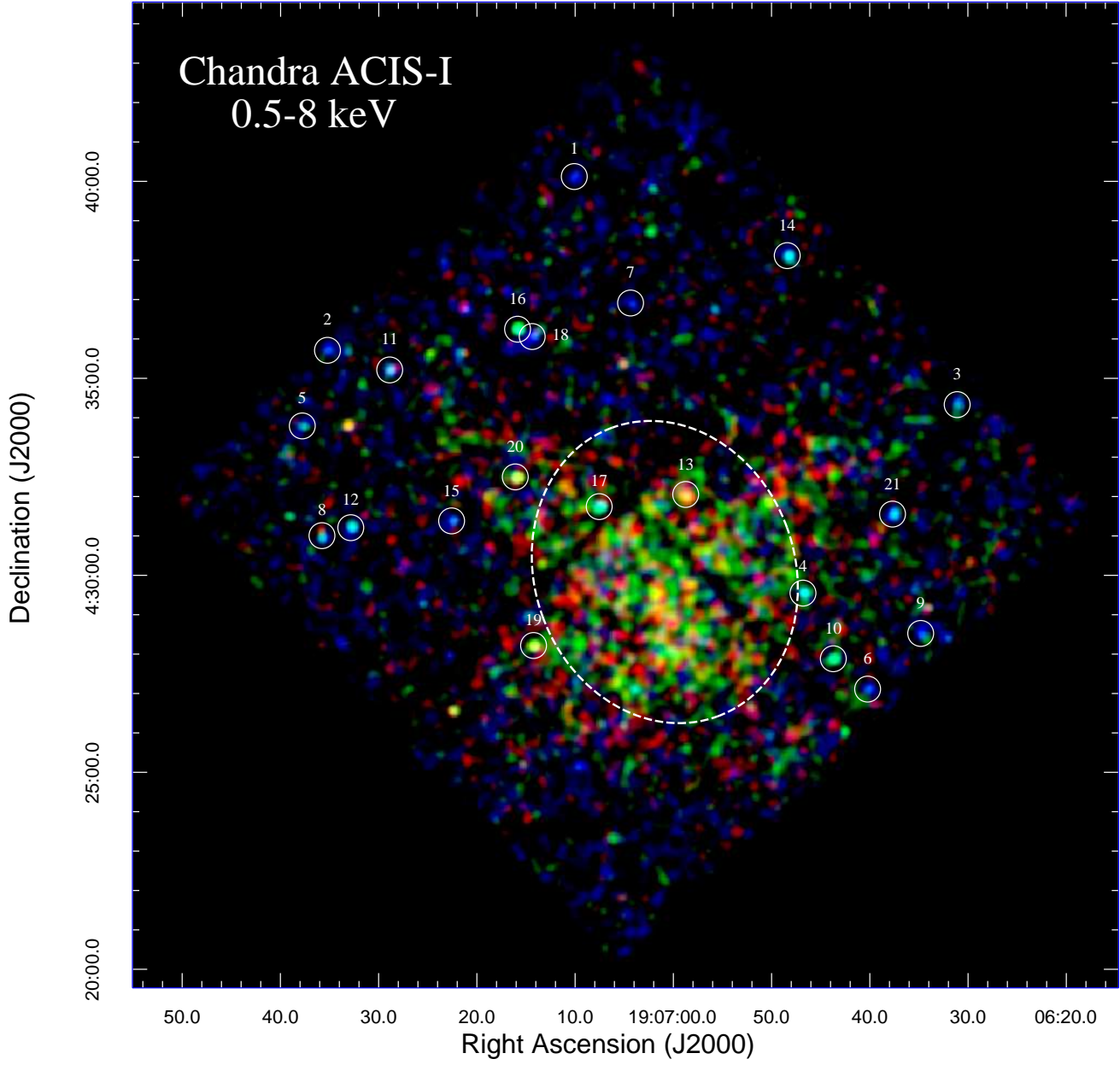


Fig. 1.— A $25' \times 25'$ X-ray color image of G38.7-1.4 as observed by Chandra ACIS-I (red: 0.5-1 keV green: 1-2 keV blue: 2-8 keV). Adaptively smoothing with a Gaussian kernel of $\sigma < 10''$ has been applied. 21 X-ray point-like sources are detected in this field. The properties of these sources are summarized in Table 1. The dashed ellipse illustrates the extraction region for the remnant spectrum in both XMM-Newton and Chandra data (see Sec. 4).

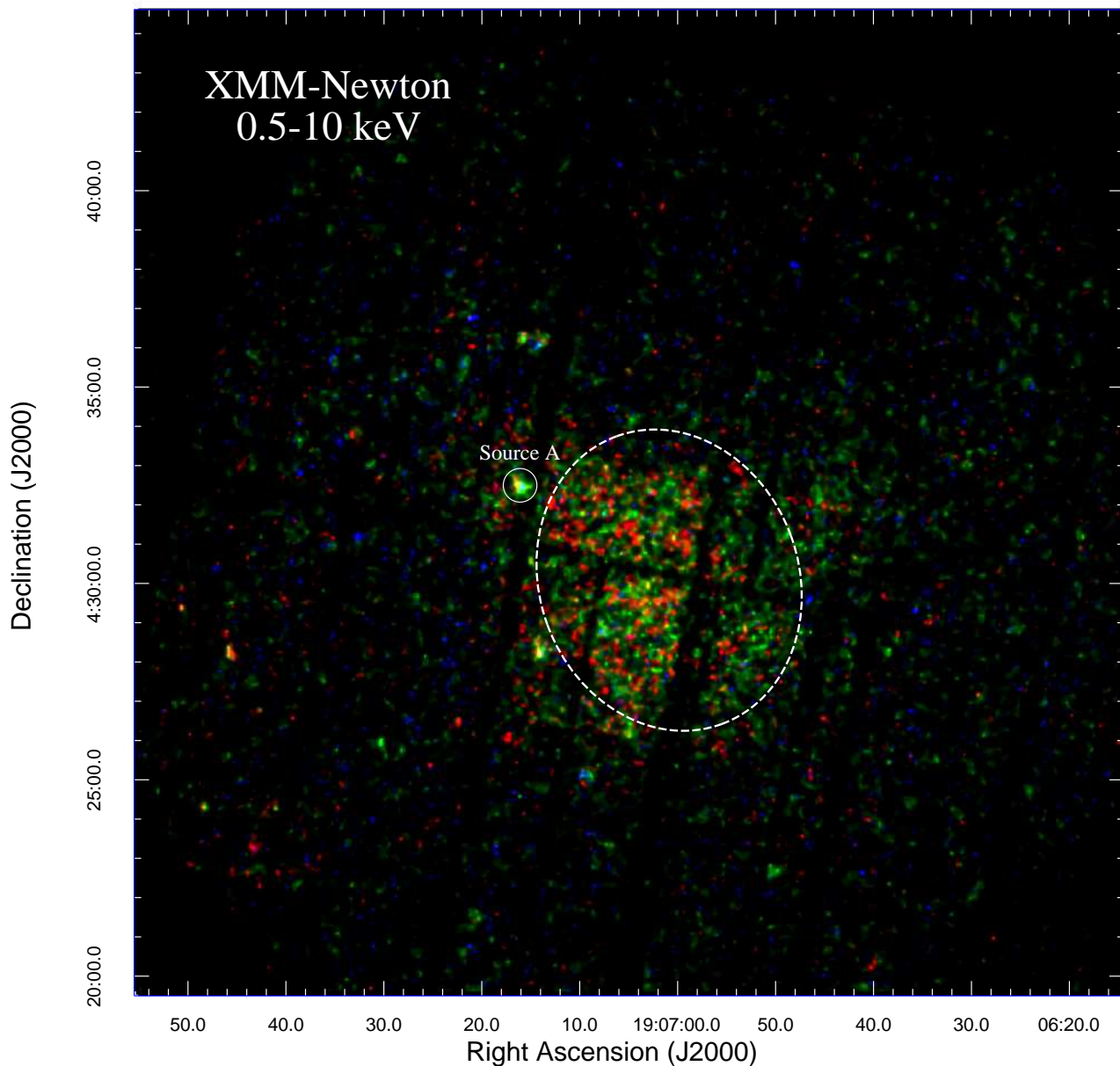


Fig. 2.— Same field-of-view as Fig 1 as observed by XMM-Newton. The X-ray color image (red: 0.5-1 keV green: 1-2 keV blue: 2-10 keV) is created by combining the data from all three cameras and has been adaptively smoothed a Gaussian kernel of $\sigma < 10''$. The dashed ellipse illustrates the extraction region for the remnant spectrum in both XMM-Newton and Chandra data (see Sec. 4). The only confirmed detection of point source in this XMM-Newton observation is labelled as “Source A” which is consistent with “Source 20” detected in the Chandra field.

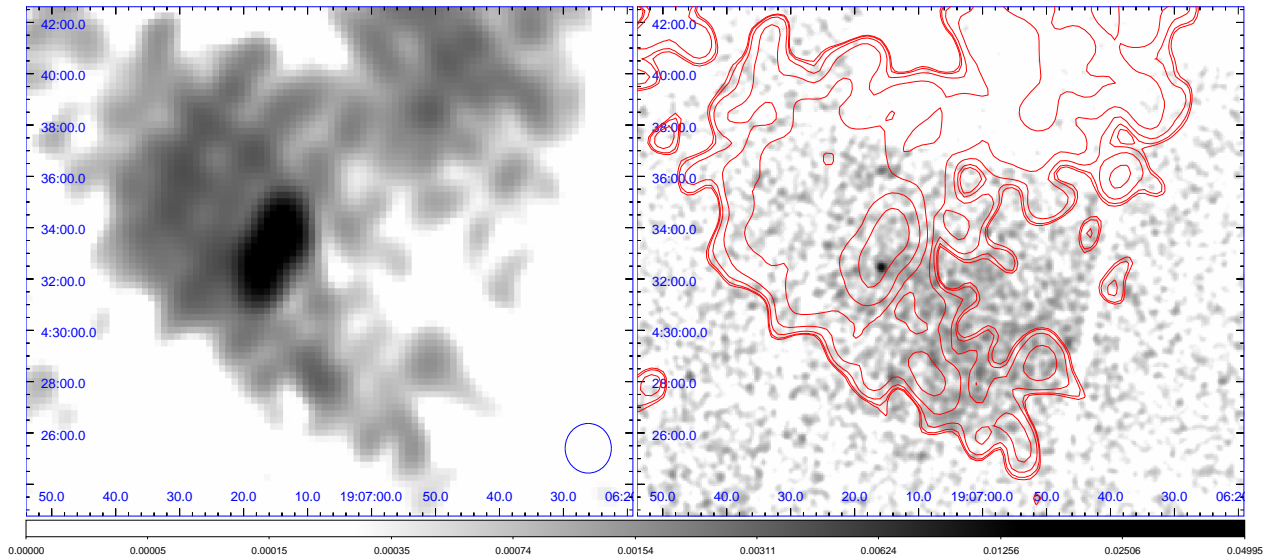


Fig. 3.— *Left panel:* 1.4 GHz VLA image of G38.7–1.4. The ellipse in the lower right corner indicates the restored beam size of $58'' \times 54''$. *Right panel:* Smoothed XMM-Newton MOS1/2 image of G38.7–1.4 superimposed with the radio contour determined as in the left panel.

determining their emission nature. Dedicated optical observations of these sources are encouraged for further investigation.

We have also computed their hardness ratios defined as $HR = (C_{2.5-8.0\text{keV}} - C_{0.5-2.5\text{keV}}) / (C_{2.5-8.0\text{keV}} + C_{0.5-2.5\text{keV}})$, where $C_{0.5-2.5\text{keV}}$ and $C_{2.5-8.0\text{keV}}$ are the net counts in the 0.5–2.5 keV and 2.5–8.0 keV energy bands. The hardness ratio of Source 13, 17 and 20 are -0.46, 0.03 and -0.82 respectively, which are rather soft. If any of these sources are indeed isolated neutron stars, their emission should be thermal dominant.

We have also attempted to search for the point sources with XMM-Newton data. A corresponding set of exposure maps was generated to account for spatial quantum efficiency, mirror vignetting, and field of view of each instrument by running the task *exmap*. Utilizing the SAS task *edetect_chain*, we performed the source detection on MOS1, MOS2 and PN images individually. We set the threshold of detection likelihood to be $m_{\text{min}}=10$ throughout the search, which corresponds to a detection significance of $\gtrsim 4\sigma$. Only one source, Source A (see Fig. 2), can be detected by all three cameras. Its position consistent with Source 20 found by Chandra (see Fig. 1). The in-

ferior performance of source detection with XMM-Newton can be ascribed to its relatively poor resolution and high instrumental background. We also noted that the brightest part of the radio emission as seen by VLA coincides with Source A (see Figure 3 right panel).

4. Spectral Analysis

We extracted the spectrum of the remnant emission from the Chandra data within the elliptical region illustrated in Fig. 1. All the detected point-like sources within the selected region (i.e. Sources 4, 13 & 17) were removed before extraction. We utilized the CIAO tool *specextract* to extract the spectra and to compute the response files. In view of low signal-to-noise ratio, the intrinsic extent of G38.7–1.4 in X-ray is uncertain. Therefore, the background spectrum is sampled from the blank-sky events. After background subtraction there are ~ 2166 net counts available in 0.5–8 keV for the spectral analysis. We binned the spectrum extracted from Chandra so as to have at least 20 counts per bin.

We utilized the XMM-Newton SAS tool *evselect* to extract the remnant spectrum from the XMM-Newton data within the same region adopted in

TABLE 1
X-RAY SOURCES IN THE FIELD OF VIEW OF CHANDRA ACIS

ID	RA (J2000) (h:m:s)	Dec (J2000) (d:m:s)	δ RA ^a (arcsec)	δ Dec ^a (arcsec)	S/N ^b σ_G	Net counts (counts)	Photon flux ^c (10^{-6} photon cm ⁻² s ⁻¹)	PSF Ratio ^d
1	19:07:10.090	+04:40:07.45	1.01	0.89	4.27	21 \pm 6	1.56 \pm 0.44	1.74
2	19:07:35.220	+04:35:42.74	0.76	0.75	4.33	23 \pm 6	1.81 \pm 0.50	1.20
3	19:06:31.099	+04:34:20.07	0.72	0.63	5.27	31 \pm 7	2.54 \pm 0.60	0.95
4	19:06:46.800	+04:29:32.99	0.14	0.28	6.68	40 \pm 8	3.50 \pm 0.71	1.45
5	19:07:37.783	+04:33:47.60	1.35	1.01	4.09	25 \pm 7	1.83 \pm 0.52	2.59
6	19:06:40.222	+04:27:06.79	0.89	1.05	4.01	22 \pm 6	1.73 \pm 0.51	2.98
7	19:07:04.356	+04:36:54.85	0.96	0.83	4.75	23 \pm 6	1.73 \pm 0.46	3.49
8	19:07:35.777	+04:31:00.48	0.54	1.13	5.03	26 \pm 6	1.96 \pm 0.49	1.92
9	19:06:34.817	+04:28:31.57	0.68	0.69	4.24	24 \pm 7	1.97 \pm 0.55	1.70
10	19:06:43.714	+04:27:53.03	0.42	0.36	4.27	22 \pm 6	1.59 \pm 0.45	1.17
11	19:07:28.884	+04:35:12.89	0.62	0.62	5.77	33 \pm 7	2.36 \pm 0.53	1.83
12	19:07:32.844	+04:31:12.61	0.65	0.76	4.97	26 \pm 7	2.03 \pm 0.51	2.20
13	19:06:58.742	+04:32:03.27	0.92	0.97	4.20	26 \pm 7	1.70 \pm 0.47	28.21
14	19:06:48.403	+04:38:06.99	0.86	0.77	6.59	36 \pm 7	2.58 \pm 0.53	2.54
15	19:07:22.577	+04:31:23.01	0.44	0.34	5.13	27 \pm 7	2.01 \pm 0.50	1.92
16	19:07:15.862	+04:36:14.94	0.62	0.58	6.22	28 \pm 6	1.87 \pm 0.42	2.82
17	19:07:07.550	+04:31:44.75	0.70	0.62	5.07	29 \pm 7	2.00 \pm 0.49	19.69
18	19:07:14.371	+04:36:03.77	0.36	0.34	7.65	43 \pm 8	3.14 \pm 0.58	1.66
19	19:07:14.232	+04:28:13.24	0.34	0.27	4.29	25 \pm 7	1.66 \pm 0.46	2.14
20	19:07:16.094	+04:32:30.02	0.55	0.59	6.69	34 \pm 7	2.24 \pm 0.46	7.55
21	19:06:37.682	+04:31:33.33	0.34	0.39	8.77	49 \pm 8	3.66 \pm 0.62	1.68

^aPosition uncertainty.

^bEstimates of source significance in units of Gehrels error: $\sigma_G = 1 + \sqrt{C_B + 0.75}$ where C_B is the background counts.

^cAbsorbed photon fluxes in the energy range of 0.5-8.0 keV.

^dThe ratios between the source extents and the estimates of the PSF sizes.

the Chandra analysis. Although Sources 4, 13 and 17 were not detected by XMM-Newton, we have removed the photons within $15''$ from their positions in order to minimize the contamination. Similarly, the background spectra for each camera were sampled from the blank-sky events. Response files were constructed by using the XMM-Newton SAS tasks *rmfgen* and *arfgen*. After background subtraction, there are 989, 1532 and 5990 net counts in 0.5–10 keV from MOS1, MOS2 and PN respectively. The extracted spectra were binned to have at least 15 for MOS1/2 and 30 for PN source counts per bin.

All the spectral fits were performed with the XSPEC software package (version: 12.7.0). All quoted errors are 1σ for 2 parameters of interest. For accounting the photoelectric absorption, we used the Wisconsin cross-sections throughout the analysis (Morrison & McCammon 1983; XSPEC model: WABS).

We began with examining the spectrum with an absorbed collisional ionization equilibrium (CIE) plasma model (XSPEC model: VEQUIL). First, we fixed the abundance of metals at the solar abundances in order to minimize the number of free parameters. We fitted the spectrum obtained from individual camera separately for checking whether the results are consistent. While the spectrum obtained from Chandra can be fitted reasonably well with the CIE model, residuals have been seen in all XMM-Newton spectra at energies $\gtrsim 2$ keV. These residuals can be modeled by including an additional power-law model in the fitting which yields a photon index of ~ 1.1 , ~ 0.3 and ~ 0.7 for MOS1, MOS2 and PN respectively. The steepness of these photon indices are inconsistent with being from a non-thermal component. Therefore, we speculate that these residuals were possibly resulted from some residual soft proton contamination in individual cameras after the data screening.

In order to tightly constrain the spectral parameters, we fitted the data obtained from all cameras simultaneously with an untied power-law component to account for the residual soft proton contamination in the XMM-Newton data. The best-fit CIE model yields a column density of $N_H = 6.85^{+0.33}_{-0.35} \times 10^{21} \text{ cm}^{-2}$ and a plasma temperature of $kT = 0.64 \pm 0.02 \text{ keV}$ (with $\chi^2 = 842.47$

for 704 degrees of freedom; hereafter dof). To examine whether the metal abundance of G38.7–1.4 deviates from the solar values, we thawed the corresponding parameters individually to see if the goodness-of-fit can be improved. With the abundances of oxygen (O) and neon (Ne) as free parameters, the fit is found to be somewhat improved ($\chi^2 = 762.43$ for 702 dof). Both O and Ne are suggested to be overabundant with respect to their solar values. The spectral parameters are tabulated in Table 2. The observed spectra with the CIE fit are display in Figure 4.

We also examined these spectra with an absorbed non-equilibrium ionization model of a constant temperature and a single ionization timescale (XSPEC model: VNEI) with the abundances of O and Ne as free parameters. The best-fit plasma temperature and the line-of-sight absorption are found to be $kT = 0.65^{+0.03}_{-0.01} \text{ keV}$ and $N_H = 5.44^{+0.33}_{-0.34} \times 10^{21} \text{ cm}^{-2}$. The abundances of O and Ne are found to be $7.63^{+1.41}_{-1.30}$ and $3.39^{+0.84}_{-0.77}$ of their solar values. All these parameters are similar to those inferred from the CIE model. The inferred ionization timescale τ_{ion} is found to be $\sim 6.8 \times 10^{12} \text{ s cm}^{-3}$, which suggests the system can possibly reach the condition for CIE already. Also, statistically, the NEI model does not provide a better description of the data than the corresponding CIE fit ($\chi^2 = 815.44$ for 701 dof). Therefore, we will not consider the NEI model in all subsequent discussions.

As the line features are not prominent in the observed energy spectra (see Fig. 4), we have also attempted to fit the data with a simple absorbed power-law model. Nevertheless, this fit yields an undesirable goodness-of-fit ($\chi^2 = 1507.73$ for 710 dof) and an unreasonable photon index of $\Gamma \sim 4.8$. And hence, this emission scenario will not be further considered.

In addition to the diffuse X-ray emission, we also examined the spectrum for the only point source detected by XMM-Newton, namely source A (see Fig. 2). The source spectrum has been extracted from a circular region with a radius of $15''$ centered at the position reported by the source detection algorithm. This choice of extraction regions corresponds to the encircled energy fraction of $\sim 70\%$. For the background subtraction, we sampled from the nearby low-count regions in the

Table 2: X-ray spectral properties of G38.7–1.4. All quoted errors are 1σ for 2 parameters of interest.

N_{H} (10^{21} cm^{-2})	$5.32^{+0.35}_{-0.32}$
kT (keV)	0.65 ± 0.03
O ^a	$7.42^{+1.50}_{-1.46}$
Ne ^a	$3.49^{+0.86}_{-0.80}$
Norm (10^{-4}) ^b	$6.32^{+0.95}_{-0.79}$
χ^2	762.43
dof	702

^a The metal abundance with respect to the solar value.

^b The model normalization is expressed as $(10^{-14}/4\pi D_A^2) \int n_e n_H dV$, where D_A is the angular diameter distance to the source (cm), n_e is the electron density (cm^{-3}), and n_H is the hydrogen density (cm^{-3}).

individual camera. There are ~ 76 net counts in total available for the spectral fitting.

In view of its softness (see Sec. 3), we first examined the spectrum of Source A with a blackbody model (XSPEC model: BBODYRAD) which yields $N_{\text{H}} = 8.20^{+3.19}_{-2.17} \times 10^{21} \text{ cm}^{-2}$ and $kT = 0.30^{+0.10}_{-0.07} \text{ keV}$ with an acceptable goodness of fit $\chi^2 = 11.37$ for 10 dof. The normalization implies an emitting region with a radius of $R < 151.45 D_{\text{kpc}} \text{ m}$, where D_{kpc} is the source distance in units of kpc. The unabsorbed flux of source A is found to be $f_x \simeq 3.9 \times 10^{-14} \text{ erg cm}^{-2} \text{ s}^{-1}$ in the energy range of 0.5–10.0 keV. We have also attempted to fit the spectrum with a power-law which results in similar a goodness of fit as the blackbody fit ($\chi^2 = 11.89$ for 10 dof). But we noted that the best-fit photon index ($\Gamma = 6.03^{+1.77}_{-1.33}$) is apparently steeper than a conventional range ($\Gamma \lesssim 3$) of acceleration processes. We have also tested a scenario that it is a clump of the diffuse emission of G38.7–1.4 by fitting a VEQUIL model to its spectrum. However, the goodness of fit is worse than the other two tested models ($\chi^2 = 12.29$ for 10 dof).

5. γ -ray Observation & Data Analysis

In order to further probe if G38.7–1.4 is a site for GCR acceleration, we searched for the γ -ray emission at its location. The Large Area Telescope (LAT) on board the Fermi Gamma-ray Space Telescope is able to detect γ -rays with energies between $\sim 100 \text{ MeV}$ and $\sim 300 \text{ GeV}$ (Atwood et al. 2009). Data used in this work were obtained between 2008 August 4 and 2012 November 21, which are available from the Fermi Science Support Center². We used the Fermi Science Tools “v9r23p1” package to reduce and analyse the data in the vicinity of G38.7–1.4.

Throughout this paper we used Pass 7 data with events in the “Source” class (i.e., event class 2) only. The corresponding instrument response functions (IRFs) “P7SOURCE_V6” (Atwood et al. 2009), which has been recommended for most analysis, was adopted. Photon energies were restricted to 200 MeV to 300 GeV. To reject atmospheric γ -rays from the Earth’s limb, we excluded the events with zenith angles larger than 100° . In order to reduce systematic uncertainties and achieve a better background modelling, a circular region-of-interest (ROI) with a diameter of 10° centered at the nominal position of G38.7–1.4 was selected in our analysis.

To investigate the γ -ray spectral characteristic of G38.7–1.4, we performed an unbinned likelihood analysis with the aid of *gtlike*, by putting a point source with a PL model at the nominal position of G38.7–1.4 (i.e. RA=19^h07^m05^s Dec=+04°31′11″ (J2000)). For the background model, we included the Galactic diffuse model (*gal_2yearp7v6_v0.fits*), the isotropic background (*iso_p7v6source.txt*), as well as all point sources reported in the Fermi LAT 2-Year Source Catalog (2FGL) within 10° from the center of the ROI. All these 2FGL sources were assumed to be point sources which have specific spectra suggested by the 2FGL catalog (Nolan et al. 2012). While the spectral parameters of the 2FGL sources locate within the ROI were set to be free, we kept the parameters for those lying outside our adopted ROI fixed at the values given in 2FGL (Nolan et al. 2012). We allowed the normalizations of diffuse background components to be free. We

²<http://fermi.gsfc.nasa.gov/ssc/data/analysis/software/>

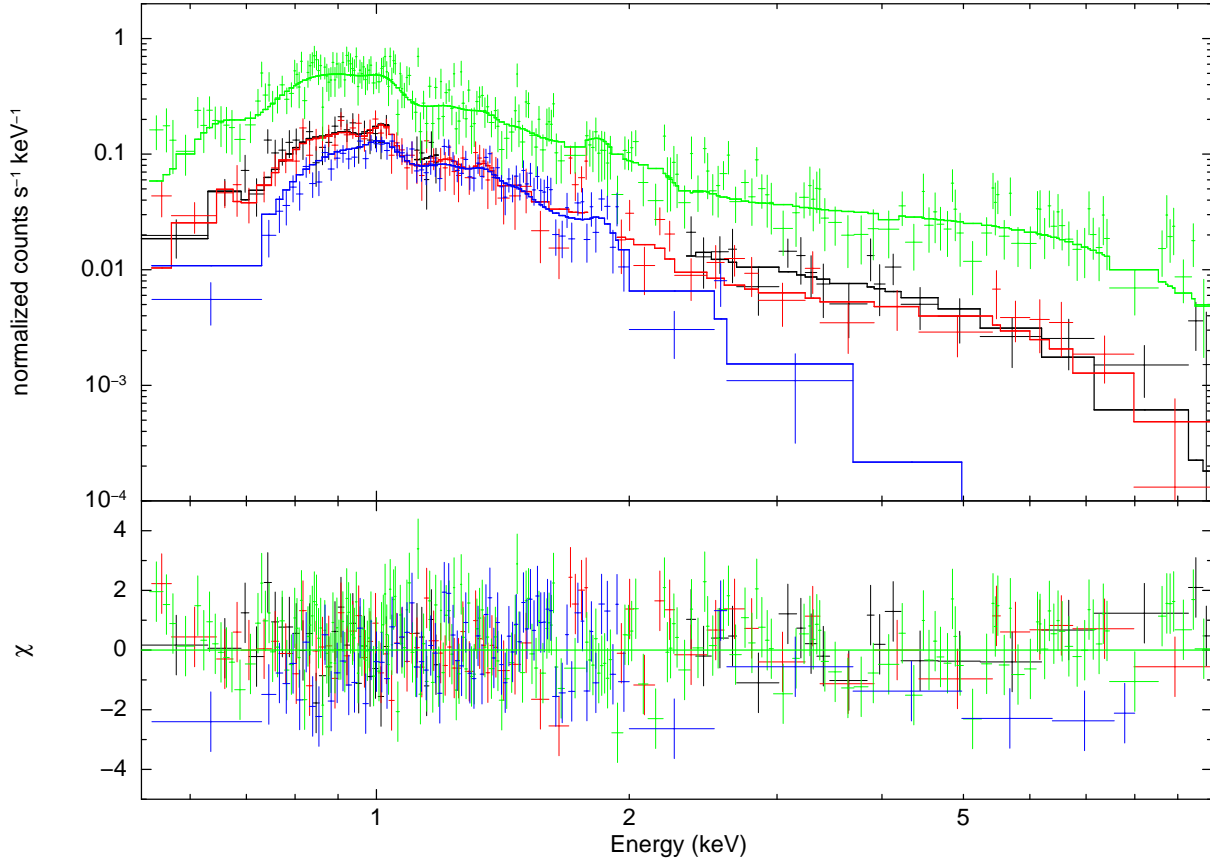


Fig. 4.— (*upper panel*) The X-ray energy spectra of G38.7–1.4 obtained from the XMM-Newton MOS1 (black), MOS2 (red), PN (green) and Chandra ACIS-I (blue) are simultaneously fitted with an absorbed collisional ionization equilibrium plasma model. Additional power-law component have been applied to account for the residual soft proton contamination in the individual XMM-Newton camera. (*lower panel*) Contributions to the χ^2 fit statistic are shown.

found that there is no γ -ray detection of G38.7–1.4 in our study ($TS = -3 \times 10^{-3}$ at the nominal position of G38.7–1.4). With the statistical uncertainties of both photon index and the prefactor concerned, the 1σ limiting photon flux at energies > 100 MeV is constrained to be $< 1.3 \times 10^{-9}$ photons $\text{cm}^{-2} \text{s}^{-1}$.

6. Discussion

Based on the best-fit X-ray spectral parameters, we discuss the physical properties of G38.7–1.4. Our analysis suggests a plasma temperature of $\sim 7.5 \times 10^6$ K which allows us to estimate the shock velocity $v_s^2 = 16kT/(3m_p\mu)$ (Reynolds 2008), where k is the Boltzmann constant, m_p is

the proton mass, μ is the mean mass per particle. For a fully ionized plasma of cosmic abundances ($\mu \sim 0.6$), the shock velocity is estimated to be $\sim 745 \text{ km s}^{-1}$.

Assuming the shocked densities of hydrogen n_H and electrons n_e are uniform in the extraction region, the normalization of the CIE model can be approximated by $10^{-14} n_e n_H V / 4\pi D^2$, where D is the distance to G38.7–1.4 in cm and V is the volume of interest in units of cm^3 . Assuming a geometry of an ellipsoid for the extraction region, the volume of interest for the SNR is $\sim 1.29 \times 10^{56} D_{\text{kpc}}^3 \text{ cm}^3$, where D_{kpc} is the remnant distance in units of kpc. Assuming a completely ionized plasma with $\sim 10\%$

He ($n_e \sim 1.2n_H$), the $1\text{-}\sigma$ confidence interval of the normalization implies that the shocked hydrogen and electron densities are in the ranges of $n_H \simeq (0.21 - 0.24)D_{\text{kpc}}^{-0.5} \text{ cm}^{-3}$ and $n_e \simeq (0.25 - 0.29)D_{\text{kpc}}^{-0.5} \text{ cm}^{-3}$, respectively.

To determine the remnant age, we assume that G38.7-1.4 is in the Sedov phase and the shocked plasma is fully ionized with a single temperature. The shock temperature can be estimated by $T \simeq 8.1 \times 10^6 E_{51}^{2/5} n_{\text{ISM}-1}^{2/5} t_4^{6/5} \text{ K}$ (Hui et al. 2012), where t_4 , E_{51} , and $n_{\text{ISM}-1}$ are the time after the explosion in units of 10^4 years, the released kinetic energy in units of 10^{51} erg , and the ISM density of 0.1 cm^{-3} , respectively. Assuming it is a strong shock, n_{ISM} is estimated to be $0.25n_H$. Taking the $1\text{-}\sigma$ uncertainties of the temperature inferred from the spectral fitting and assuming $E_{51} = 1$ and a distance of 4 kpc, the age of G38.7-1.4 is constrained to be $(1.1 - 1.2)D_{\text{kpc}}^{1/6} \times 10^4$ years.

Since the distance plays a crucial role in determining the physical properties of a SNR, to estimate the distance of G38.7-1.4 is essential in our study. We first tried to obtain the distance at the lower side via the optical extinction. Lucke (1978) built contour plots of equal mean reddening up to 2 kpc and found the mean color excess $E_{B-V} = 0.25 \text{ mag kpc}^{-1}$ by using color excess and photometric distances in the UB system for 4000 OB stars. From studies using ultraviolet spectroscopy of reddened stars and X-ray scattering halos in our Galaxy, Predehl & Schmitt (1995) found the relationship between N_H and the total extinction $A(V)$ to be approximately $N_H/A(V) = 1.79 \times 10^{21} \text{ cm}^{-2}$. Adopted the $N_H \sim 5.3 \times 10^{21}$ inferred from the spectral fitting (cf. Table 2) and a typical value of 3.1 for $A(V)/E_{B-V}$ in the Milky Way, we can crudely estimate a distance of $\sim 4 \text{ kpc}$. A dedicated HI observation of this newly identified SNR is encouraged for a more reliable distance estimation.

Non-detection of γ -ray emission in the energy range of $0.2 - 300 \text{ GeV}$ at the nominal position of G38.7-1.4 was reported in our study. We have placed a limiting photon flux of $F(\geq 100 \text{ MeV}) < 1.3 \times 10^{-9} \text{ photons cm}^{-2} \text{ s}^{-1}$. Using the parameters inferred from the aforementioned X-ray analysis, we can estimate what is the expected intensity of the γ -ray flux from G38.7-

1.4. From Drury et al. (1994), the theoretical γ -ray flux can be estimated as $F(\geq 100 \text{ MeV}) \approx 4.4 \times 10^{-7} \theta \left(\frac{E_{\text{SN}}}{10^{51} \text{ erg}}\right) \left(\frac{d}{1 \text{ kpc}}\right)^{-2} \left(\frac{n}{1 \text{ cm}^{-3}}\right) \text{ cm}^{-2} \text{ s}^{-1}$. Adopting a distance of $d \sim 4 \text{ kpc}$, the ambient density of $n = n_{\text{ISM}} \sim 0.05 \text{ cm}^{-3}$ as inferred from X-ray spectral fit and assuming a canonical explosion energy of $E_{\text{SN}} \sim 10^{51} \text{ ergs}$ which converts $\theta = 10\%$ into GCR energy (cf. Kang 2013), a flux of $F(\geq 100 \text{ MeV}) \sim 1.4 \times 10^{-10} \text{ cm}^{-2} \text{ s}^{-1}$ is expected from G38.7-1.4. A deeper γ -ray search is encouraged for further probing whether G38.7-1.4 is an acceleration site of GCRs indeed.

7. Summary & Conclusion

We have performed a detailed spectro-imaging X-ray study of the supernova remnant candidate G38.7-1.4 with XMM-Newton and Chandra. A central-filled X-ray structure correlated with an incomplete radio shell has been revealed. Its X-ray spectrum is thermal dominated and has shown the presence of a hot plasma accompanied with metallic emission lines. These observed properties indicate that G38.7-1.4 is a SNR belong to a mix-morphology category. The enhanced abundances of O and Ne suggest G38.7-1.4 might be resulted from a core-collapsed SN. We have also searched for the possible γ -ray emission from G38.7-1.4 with *Fermi* LAT data. With the adopted ~ 4.3 yrs data span in this study, we report a non-detection of any γ -ray emission in the energy range of $0.2 - 300 \text{ GeV}$.

This project is supported by the National Science Council of the Republic of China (Taiwan) through grant NSC100-2628-M-007-002-MY3 and NSC100-2923-M-007-001-MY3. CYH and KAS are supported by the National Research Foundation of Korea through grant 2011-0023383. LT would like to thank the German *Deutsche Forschungsgemeinschaft (DFG)* for financial support in project SFB TR 7 Gravitational Wave Astronomy.

REFERENCES

- Atwood, W. B., et al. 2009, ApJ, 697, 1071
- Boss, A. P. 1995, ApJ, 439, 224
- Caprioli, D. 2011, JCAP, 5, 26

- Chieffi A., & Limongi, M. 2004, *ApJ*, 608, 405
- Drury, L. O., Aharonian, F. A., & Voelk, H. J. 1994, *A&A*, 287, 959
- Ferrand, G., & Safi-Harb, S. 2012, *Advances in Space Research*, 49, 1313
- Gaustad, J. E., McCullough, P. R., Rosing, W., & Van Buren, D. 2001, *PASP*, 113, 1326
- Green, D. A. 2009, *Bulletin of the Astronomical Society of India*, 37, 45
- Green, P. J., et al. 2004, *ApJS*, 150, 43
- Haberl, F. 2007, *Ap&SS*, 308, 181
- Hui, C. Y. 2013, *JASS*, 30, 127
- Hui, C. Y., Seo, K. A., Huang, R. H. H., Trepl, L., Woo, Y. J., Lu, T.-N., Kong, A. K. H., & Walter, F. M. 2012, *ApJ*, 750, 7
- Kalberla, P. M. W., Burton, W. B., Hartmann, D., Arnal, E. M., Bajaja, E., Morras, R., & Pöppel, W. G. L. 2005, *A&A*, 440, 775
- Kang, H. 2013, *JASS*, 30, 133
- Lucke, P. B. 1978, *A&A*, 64, 367
- Maccacaro, T., Gioia, I. M., Wolter, A., Zamorani, G., & Stocke, J. T. 1988, *ApJ*, 326, 680
- Morrison, R., & McCammon, D. 1983, *ApJ*, 270, 119
- Nolan, P. L., et al. 2012, *VizieR Online Data Catalog*, 219, 90031
- Predehl, P., & Schmitt, J. H. M. M. 1995, *A&A*, 293, 889
- Reynolds, S. P. 2008, *ARA&A*, 46, 89
- Schaudel, D., Becker, W., Voges, W., Aschenbach, B., Reich, W., & Weisskopf, M. 2002, in *Astronomical Society of the Pacific Conference Series*, Vol. 271, *Neutron Stars in Supernova Remnants*, ed. P. O. Slane & B. M. Gaensler, 391
- Sinnis, G. et al. 2009, *Astro2010: The Astronomy and Astrophysics Decadal Survey*, *Science White Papers*, no. 275
- Stocke, J. T., Morris, S. L., Gioia, I. M., Maccacaro, T., Schild, R., Wolter, A., Fleming, T. A., & Henry, J. P. 1991, *ApJS*, 76, 813
- Tammann, G. A., Loeffler, W., & Schroeder, A. 1994, *ApJS*, 92, 487
- Thielemann, F. K., et al. 1996, *ApJ*, 460, 408
- Woosley, S. E., & Weaver, T. A. 1995, *ApJS*, 101, 181
- Wright, E. L., et al. 2010, *AJ*, 140, 1868